Office of Naval Research
Quantum-enhanced FAST CARS for remote detection using a multi-static platform
Award Number N00014-20-1-2086
Project Period 03/01/2020 through 02/28/2023
Final Technical Report

Principal Investigator: Dr. Svetlana A. Malinovskaya
Department of Physics
Stevens Institute of Technology
Hoboken, NJ 07030
Ph.:(201) 216-8094, (734) 717-3604
Fax: (201) 216-5638
e-mail: smalinov@stevens.edu

I. SUMMARY

Remote detection of particular matter in the atmosphere is both an important and challenging problem. Potentially hazardous material can be released onto the atmosphere by an enemy plane which would require immediate detection and action. Remote detection can also be used to extract information about magnetic fields using sodium atoms in the mesosphere. In common methods, the detected signal is small because the signal suffers from losses proportionally to the inverse squared distance. The loss is caused by the fact that the backscattered light fills a semi-sphere that propagates out. In this project we developed a new, quantum-enabled approach to increase the signal at the detector by depending on a process which is directional. It is based on coherent anti-Stokes Raman scattering (CARS) of laser radiation from the distant molecules in the backward direction. The quantum enhancement is achieved through the implementation of the newly developed quantum control methodology, which maximizes quantum coherence in the target molecules. Coherent signal in the backward direction is sustained by application of phase locked pulse trains

which form optical frequency combs. The implementation of quantum control methods in combination with optical frequency combs in CARS for remote detection presents a fundamentally new approach within Femtosecond Adaptive Spectroscopic Techniques (FAST CARS). Each pulse in the pulse train is analyzed and controlled using the deep learning algorithm. Deep neural networks are used to analyze the modulation of the phase of the laser fields propagating through the air and aids in making adjustments to the control algorithm for the laser fields. The detection principle relies on nonlinear optical response of the target molecules, when a blue-shifted with respect to the incident fields radiation is generated coherently in the medium and propagates in the direction defined by the phase-matching condition in the four-wave mixing of CARS. The configuration of the laser beams implies the BOX type, with the anti-Stokes signal emerging from the fourth corner. This is so called FAST BOXCARS, a laser configuration, which is applicable on a multi-static platform such as nearby inflatables or unmanned aerial vehicles (drones). We demonstrated a significant enhancement of the signal using the developed quantum control approach. This method is ready for application within the multi-static platform laser configuration. The completion of proposed work advanced understanding of the limits of realization of FAST BOXCARS for the remote detection of hazardous air contaminants and demonstrated the enhancement of the anti-Stokes component of the filed forming the backscattered signal sufficient for the standoff detection.

The main results were published in the leading, peer reviewed journals [1–4], two book chapters [5, 6], they were presented at multiple scientific conferences and discussed during scientific visits of universities. Additional peer reviewed journal publications are [7–10]. Altogether, we have published ten papers in the top research journals, such as Quantum Science and Technology, Nature Scientific Reports, Chemical Physics Letters, Advances in Theoretical and Computational Physics. Two PhD students and one undergraduate student were working on the project. On December 8th, 2022, PhD student Jabir Chathanathil defended his Dissertation titled "Chriped pulse control of quantum coherence in atoms and molecules: A semiclassical theory with applications for detection and sensing." He graduated with PhD in Physics and received the PhD Thesis Award 2023 in the Department of Physics at Stevens Institute of Technology.

II. RESULTS

Background: Coherent anti-Stokes Raman scattering (CARS) belongs to the frontiers of non-linear optics methods suited for imaging, sensing and detection without labeling or destruction [11]. The implementation of ultrafast pulses in the stimulated Raman spectroscopy in general and CARS in particular brings advantages of the high peak power, the three-dimensional spacial resolution, and the femtosecond time resolution to monitor vibrational dynamics [12–15]. Femtosecond CARS has been widely used and nowadays advances toward solving tasks related to a single molecule spectroscopy, molecular specific imaging, sensing traces of molecules and remote detection. Success in these areas depends on a high level of chemical sensitivity and specificity, the signal to noise ratio, and the CARS signal intensity. Because the Raman fields' evolution is proportional to the macroscopic induced polarization [16], which in its turn is proportional to a microscopic quantum property of the material, quantum coherence, crafting ultrafast laser pulses to generate the maximum coherence in the target molecules is the root to impact the molecular-specific response and to significantly enhance the signal. To date, there has been a number of methods developed to achieve the maximum coherence leading to the enhancement of the signal from predetermined vibrational modes in CARS using the shaped ultrafast pulses. Among pioneering works including those for remote detection are [17–19], [20, 21] and [22, 23] proposing different phase shaping of the ultrafast pulses. Other notable works are the multiplex CARS using a combination of a narrow-band chirped pump and probe and a transform-limited broadband Stokes pulse [24] and a proposal of double parabolic phase functions in the stimulated Raman scattering (SRS) [25].

The novelty of our approach is i) in using the specifically chirped incident pulse trains to reach adiabatic regime of light-matter interaction during the propagation aiming at a creation of the maximum vibrational coherence, ii) in utilizing the pulse train properties to mitigate decoherence and iii) in implementing the deep convolution networks approach to evaluate the phase of the propagating fields, which provides with the information about the relative phase change between the pump, the Stokes, the probe and the anti-Stokes pulses. Our method demonstrated the built-up of the anti-Stokes signal which is a molecular signature in the backward CARS radiation. Our method can be also used for the multiplex CARS by fixing the central pump frequency and scanning the Stokes frequency to obtain

the vibrational spectrum of unknown species. In contrast to the multiplex CARS in [24], our method provides the maximum CARS signal for each instantaneous magnitude of the Stokes central frequency and efficiently suppresses the background signal. Using a time delay between two equally chirped pulses in CARS in [26] as a way to tune two-photon detuning into resonance, gives rise to the time-dependent ac Stark shifts leading to nondiabatic type of light-matter interaction [15]. Such method is sensitive to the pulse parameters and the selectivity is limited by nonadiabatic coupling. In contrast, our method makes use of the advantage of adiabatic passage and may provide a robust way to control vibrational coherence at a distance.

As a case study we use the methanol vapor. Methanol molecules have Raman active symmetric 2837 cm^{-1} (85.05 THz) and asymmetric 2942 cm^{-1} (88.20 THz) stretch modes. These values are within the range of molecular group vibrations in various biochemical species, which span from 2800 to 3100 cm^{-1} making the methanol a suitable choice as a surrogate molecule for non-hazardous experiments in the lab. Thus, the results of methanol studies would be useful for the development of remote detection schemes as well as for the environmental analyses.

Various setups are available to perform CARS experiments satisfying the phase-matching conditions to separate the directional anti-Stokes signal from the incident fields. However for particles having a size comparable to the wavelength, the phase-mismatched factor is small and it was shown that the non-phase-matched CARS can provide an effective method to probe complex molecules [19, 27]. For methanol, the ratio $4\pi\rho_0/\lambda \ll 1$, where $\rho_0 \sim 10^{-10}m$ is the target molecule diameter; it relaxes the phase-matching condition and permits consideration of the collinear copropagating fields configuration.

III. THEORETICAL FRAMEWORK

A. Maxwell - Liouville von Neumann formalism

CARS is a third order nonlinear process in which three beams, the pump, the Stokes and the probe, at frequencies ω_p, ω_s and ω_{pr} respectively, interact with the electronic vibrational - vibronic - states of the target molecules to generate the anti-Stokes field at frequency $\omega_{as} = \omega_p + \omega_{pr} - \omega_s$, Fig(1). In our control scheme, we use linearly chirped pulse trains

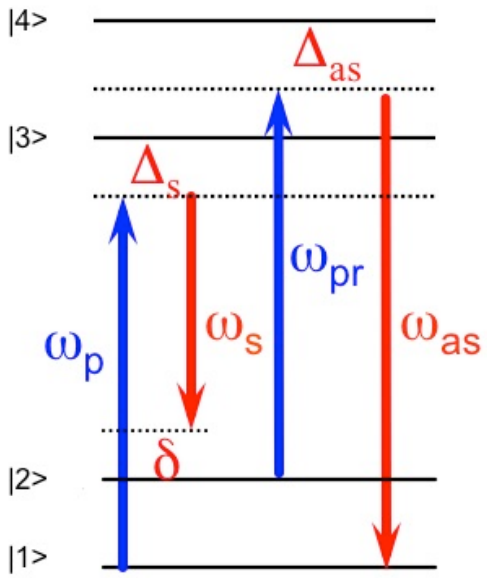

FIG. 1: Schematic of CARS: the pump (ω_p) and the Stokes (ω_s) fields interact with the ground $|1\rangle$ and the excited $|2\rangle$ vibronic states of the target molecule to create a superposition state with coherence ρ_{12}. The probe (ω_{pr}) field interacts with this superposition state to generate anti-Stokes field at frequency ω_{as}. Parameters Δ_s and Δ_{as} are the one-photon detunings, and δ is the two-photon detuning.

which read

$$E(t) = \sum_{k=0}^{N-1} E_0 exp\{-\frac{(t-t_c-kT)^2}{2\tau^2}\}\cos\{\omega_0(t-t_c-kT)+\alpha_i\frac{(t-t_c-kT)^2}{2}\}. \qquad (1)$$

Here T is the pulse train period, t_c is the central time when the peak value of the Gaussian field envelope is E_0, τ is the pulse duration, ω_0 is the carrier frequency, and α_i, $i = p, s, pr$, is the linear chirp rate of an individual pump, Stokes and probe pulse in the respective pulse train. The values of α_i are chosen in accordance with the control scheme, which implies $\alpha_s = -\alpha_p$ and $\alpha_{pr} = \alpha_s - \alpha_p$ for $t \leq t_c$; and $\alpha_s = \alpha_p$ and $\alpha_{pr} = 0$ for $t > t_c$ [3].

Such chirped pulses induce the maximum coherence between vibronic states in the target molecules via adiabatic passage provided the two-photon detuning $\delta = 0$. Any slightly different vibrational mode not satisfying the two-photon resonance condition, $\delta \neq 0$, is suppressed. The selectivity of the mode excitation is determined by the condition $\tau\delta \geq 1$, where τ is the ultrafast chirped pulse duration.

The matrix Hamiltonian written in the interaction representation reads

$$H = \frac{\hbar}{2}\begin{pmatrix} 0 & 0 & \Omega_{p_0}(t)e^{i\Delta_s t + i\frac{\alpha_p}{2}t^2} & \Omega_{as_0}(t)e^{i\Delta_{as}t} \\ 0 & 0 & \Omega_{s_0}(t)e^{i\Delta_s t + i\frac{\alpha_s}{2}t^2} & \Omega_{pr_0}(t)e^{i\Delta_{as}t + i\frac{\alpha_{as}}{2}t^2} \\ \Omega^*_{p_0}(t)e^{-i\Delta_s t - i\frac{\alpha_p}{2}t^2} & \Omega^*_{s_0}(t)e^{-i\Delta_s t - i\frac{\alpha_s}{2}t^2} & 0 & 0 \\ \Omega^*_{as_0}(t)e^{-i\Delta_{as}t} & \Omega^*_{pr_0}(t)e^{-i\Delta_{as}t - i\frac{\alpha_{as}}{2}t^2} & 0 & 0 \end{pmatrix} \quad (2)$$

Here $\Omega_{p_0}(t) = -\mu_{31}/\hbar E_{p_0}(t)$, $\Omega_{s_0}(t) = -\mu_{32}/\hbar E_{s_0}(t)$, $\Omega_{pr_0}(t) = -\mu_{42}/\hbar E_{pr_0}(t)$, $\Omega_{as_0}(t) = -\mu_{41}/\hbar E_{as_0}(t)$ are the Rabi frequencies of respective fields, μ_{ij} is a dipole moment, Δ_s and Δ_{as} are the one-photon detunings on transitions $|1\rangle \rightarrow |3\rangle$ and $|1\rangle \rightarrow |4\rangle$ respectively.

To account for the propagation effects in the scattering process, we combine the Liouville von Neumann equation for the states with Maxwell's equations for the fields. The displacement current is determined as $D = \epsilon_0 E + P$, where P is the expectation value of the induced dipole moment and ϵ_0 is the permittivity of free space. The effects arising from magnetization are neglected giving $B = \mu_0 H$, where μ_0 is permeability of free space. With no free currents and charges, Maxwell's equations read

$$\nabla \cdot (\epsilon_0 E + P) = 0 \quad (3)$$

$$\nabla \times E = -\partial B/\partial t \quad (4)$$

$$\nabla \times B = \mu_0 \partial(\epsilon_0 + P)/\partial t \quad (5)$$

$$\nabla \cdot B = 0 \quad (6)$$

From Eqs.(4,5) we obtain the wave equation

$$\nabla^2 E - \epsilon_0\mu_0 \frac{\partial^2 E}{\partial^2 t} = \nabla(\nabla \cdot E) + \mu_0 \frac{\partial^2 P}{\partial^2 t}. \quad (7)$$

It follows from Eq.(3) that $\nabla \cdot E = \nabla \cdot P/\epsilon_0$ in a space free from charges. In a plane wave limit, when the wave length is much less than the beam radius and neglecting any diffraction effects in transverse direction, fields propagate in the $\hat{z}$ direction and have polarization in

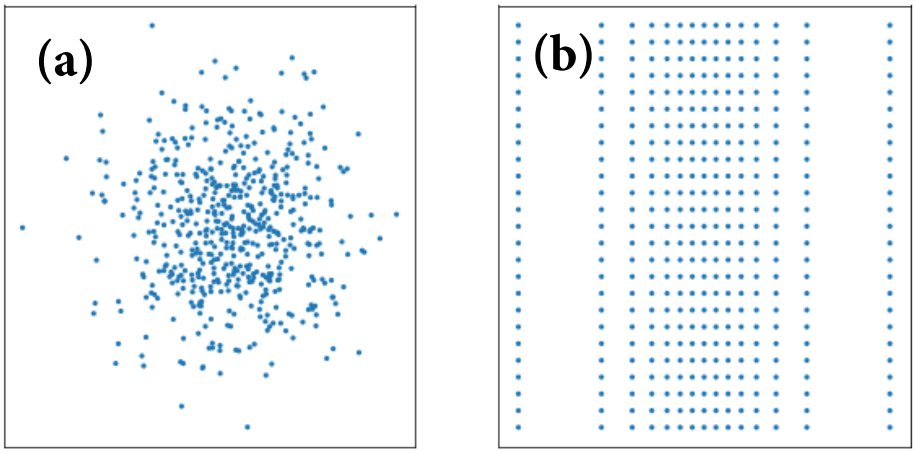

FIG. 2: The Gaussian distribution of the target molecules in (a) based on the density of molecules and in (b) is converted into multi-layer model. Each layer in the multi-layer model is characterized by the fractional number density η and a distance to it adjacent layer $(\Delta z)_\eta$. If N_s is the number of the target molecules and N is the number of total molecules associated with the layer, the fractional number density of that layer is defined as $\eta = N_s/N$. The distance between the adjacent layers $(\Delta z)_\eta$ changes according to the Gaussian distribution of molecules. The incoming pulses pass through a series of scattering events with the target molecules within each layer to produce a detectable backscattered CARS signal.

the XY plane. Then $\nabla \cdot P$ may be set to zero and the wave equation reads

$$\left(\frac{\partial}{\partial z} + \frac{1}{c}\frac{\partial}{\partial t}\right)\left(-\frac{\partial}{\partial z} + \frac{1}{c}\frac{\partial}{\partial t}\right) E = -\mu_0 \frac{\partial^2 P}{\partial t^2} \tag{8}$$

Assuming the field is $E(z,t) = \frac{1}{2}(E_0(z,t)e^{-i[\omega t - kz - \phi(z,t)]} + c.c)$ and polarization is $P(z,t) =$

$\frac{1}{2}(P_0(z,t)e^{-i[\omega t-kz-\phi(z,t)]}+c.c)$ and considering $E_0(z,t)$ and $\phi(z,t)$ as slowly varying functions of position and time, we write

$$-\frac{\partial E(z,t)}{\partial z} = -\frac{1}{2}(e^{-i\omega t}e^{ikz}e^{i\phi(z,t)}\frac{\partial E_0(z,t)}{\partial z} + ikE_0(z,t)e^{-i\omega t}e^{ikz}e^{i\phi(z,t)} + i\frac{\partial \phi(z,t)}{\partial z}E_0(z,t)e^{-i\omega t}e^{ikz}e^{i\phi(z,t)} + c.c.) \tag{9}$$

$$\frac{1}{c}\frac{\partial E(z,t)}{\partial t} = \frac{1}{2c}(e^{-i\omega t}e^{ikz}e^{i\phi(z,t)}\frac{\partial E_0(z,t)}{\partial t} - i\omega E_0(z,t)e^{-i\omega t}e^{ikz}e^{i\phi(z,t)} + i\frac{\partial \phi(z,t)}{\partial t}E_0(z,t)e^{-i\omega t}e^{ikz}e^{i\phi(z,t)} + c.c.) \tag{10}$$

Then

$$\begin{aligned}\left(-\frac{\partial}{\partial z}+\frac{1}{c}\frac{\partial}{\partial t}\right)E &= -\frac{ik}{2}(E_0(z,t)e^{-i\omega t}e^{ikz}e^{i\phi(z,t)} - c.c.) \\ &\quad -\frac{i\omega}{2c}(E_0(z,t)e^{-i\omega t}e^{ikz}e^{i\phi(z,t)} - c.c.) \\ &= -ik(E_0(z,t)e^{-i(\omega t-kz-\phi(z,t))} + c.c.) = -2ik\,\mathrm{Im}\{E\}.\end{aligned} \tag{11}$$

By substituting Eq.(11) to Eq.(8) and using $\omega/c = k$ and later assuming real fields we arrive at

$$\begin{aligned}&-ik\left(\tfrac{\partial}{\partial z}+\tfrac{1}{c}\tfrac{\partial}{\partial t}\right)(E_0(z,t)e^{-i(\omega t-kz-\phi(z,t))} + c.c.) = \\ &-ik\tfrac{\partial E_0(z,t)}{\partial z}e^{-i(\omega t-kz-\phi(z,t))} + ik\tfrac{\partial E_0^*(z,t)}{\partial z}e^{i(\omega t-kz-\phi(z,t))} \\ &-\tfrac{ik}{c}\tfrac{\partial E_0(z,t)}{\partial t}e^{-i(\omega t-kz-\phi(z,t))} + \tfrac{ik}{c}\tfrac{\partial E_0^*(z,t)}{\partial t}e^{i(\omega t-kz-\phi(z,t))} = \\ &-ik\left[\left(\tfrac{\partial E_0(z,t)}{\partial z}+\tfrac{1}{c}\tfrac{\partial E_0(z,t)}{\partial t}\right)e^{-i(\omega t-kz-\phi(z,t))} - \left(\tfrac{\partial E_0^*(z,t)}{\partial z}+\tfrac{1}{c}\tfrac{\partial E_0^*(z,t)}{\partial t}\right)e^{i(\omega t-kz-\phi(z,t))}\right] = \\ &-2k\left(\tfrac{\partial E_0(z,t)}{\partial z}+\tfrac{1}{c}\tfrac{\partial E_0(z,t)}{\partial t}\right)\tfrac{1}{2i}\left(-e^{-i(\omega t-kz-\phi(z,t))}+e^{i(\omega t-kz-\phi(z,t))}\right) \\ &= -2k\left(\tfrac{\partial E_0(z,t)}{\partial z}+\tfrac{1}{c}\tfrac{\partial E_0(z,t)}{\partial t}\right)\sin(\omega t-kz-\phi(z,t)) = \\ &-\mu_0\tfrac{\partial^2}{\partial t^2}P(z,t)\end{aligned} \tag{12}$$

For $P(z,t) = \frac{1}{2}(P_0(z,t)e^{-i[\omega t-kz-\phi(z,t)]} + c.c)$,

$$\frac{\partial^2}{\partial t^2}P(z,t) = -\omega^2\left(\frac{1}{2}(P_0(z,t)e^{-i[\omega t-kz-\phi(z,t)]} + c.c)\right) = -\omega^2\,\mathrm{Re}\left[P(z,t)\right] \tag{13}$$

Substituting these in Eq.(12) gives

$$\begin{aligned}&-2k(\tfrac{\partial E_0(z,t)}{\partial z}+\tfrac{1}{c}\tfrac{\partial E_0(z,t)}{\partial t})\sin(\omega t-kz-\phi(z,t)) = \\ &\mu_0\omega^2\left(Re\left[P_0(z,t)\right]\cos(\omega t-kz) + Im\left[P_0(z,t)\right]\sin(\omega t-kz-\phi(z,t))\right),\end{aligned} \tag{14}$$

leading to

$$-2k(\tfrac{\partial E_0(z,t)}{\partial z}+\tfrac{1}{c}\tfrac{\partial E_0(z,t)}{\partial t})=\ \mu_0\omega^2 Im\left[P_0(z,t)\right]. \tag{15}$$

In quantum theory, a measurable quantity is the expectation value, which for macroscopic polarization is an expectation value of the electric dipole moment operator $\hat{\mu}$, $\langle P(z,t)\rangle = N_s Tr\{\langle\rho(z,t)\cdot\mu\rangle\}$, where N_s is the atomic density of the target molecules. Applied to the four-level system of CARS, it contains four components corresponding to each of four transitions:

$$\begin{aligned}
P_p(z,t) &= 2N_s\,\mathrm{Re}\left[\mu_{13}\rho_{13}(z,t)e^{i(\omega_p t-k_p z-\phi(z,t))}\right]\\
P_s(z,t) &= 2N_s\,\mathrm{Re}\left[\mu_{23}\rho_{23}(z,t)e^{i(\omega_s t-k_s z-\phi(z,t))}\right]\\
P_{pr}(z,t) &= 2N_s\,\mathrm{Re}\left[\mu_{24}\rho_{24}(z,t)e^{i(\omega_{pr} t-k_{pr} z-\phi(z,t))}\right]\\
P_{as}(z,t) &= 2N_s\,\mathrm{Re}\left[\mu_{14}\rho_{14}(z,t)e^{i(\omega_{as} t-k_{as} z-\phi(z,t))}\right],
\end{aligned} \tag{16}$$

giving $P_{0p}(z,t)=N_s\mu_{13}\rho_{13}(z,t)$, $P_{0s}(z,t)=N_s\mu_{23}\rho_{23}(z,t)$, $P_{0pr}(z,t)=N_s\mu_{24}\rho_{24}(z,t)$, and $P_{0as}(z,t)=N_s\mu_{14}\rho_{14}(z,t)$.

For four components of propagating fields in CARS, the Eq.(15) reads as follows

$$\begin{aligned}
\tfrac{\partial E_p}{\partial z}+\tfrac{1}{c}\tfrac{\partial E_p}{\partial t} &= -N_s\tfrac{\mu_0\mu_{13}\omega_p^2}{k_p}\,\mathrm{Im}\{\rho_{13}(z,t)\}\\
\tfrac{\partial E_s}{\partial z}+\tfrac{1}{c}\tfrac{\partial E_s}{\partial t} &= -N_s\tfrac{\mu_0\mu_{23}\omega_s^2}{k_s}\,\mathrm{Im}\{\rho_{23}(z,t)\}\\
\tfrac{\partial E_{pr}}{\partial z}+\tfrac{1}{c}\tfrac{\partial E_{pr}}{\partial t} &= -N_s\tfrac{\mu_0\mu_{24}\omega_{pr}^2}{k_{pr}}\,\mathrm{Im}\{\rho_{24}(z,t)\}\\
\tfrac{\partial E_{as}}{\partial z}+\tfrac{1}{c}\tfrac{\partial E_{as}}{\partial t} &= -N_s\tfrac{\mu_0\mu_{14}\omega_{as}^2}{k_{as}}\,\mathrm{Im}\{\rho_{14}(z,t)\}.
\end{aligned} \tag{17}$$

If $\tau=(t-\frac{z}{c})$, then $\frac{\mathrm{d}t}{\mathrm{d}z}=(\frac{\mathrm{d}\tau}{\mathrm{d}z}+\frac{1}{c})$, which leads to $\frac{\partial}{\partial z}=\frac{\partial}{\partial t}\frac{\partial t}{\partial z}=\frac{1}{c}\frac{\partial}{\partial t}$. Taking into account that $k_q=\omega_q/c$, and $c\omega_q\hbar=E_q$, where $q=p,s,pr,as$, the Eq. (17) becomes

$$\frac{1}{c}\frac{\partial E_q}{\partial t}=-N_s\mu_0\mu_{ij}\frac{E_q(t)}{\hbar}\,\mathrm{Im}\{\rho_{ij}\} \tag{18}$$

Solving the Liouville von Neumann equation $i\hbar\dot{\rho}=[H,\rho]$ for the above Hamiltonian, and using the rotating wave approximation and adiabatic elimination of the excited states such that $\dot{\rho}_{13},\dot{\rho}_{14},\dot{\rho}_{23},\dot{\rho}_{24},\dot{\rho}_{34}\approx 0,\ \rho_{34}\approx 0,\ \rho_{33},\rho_{44}\ll\rho_{11},\rho_{22}$ and $\dot{\rho}_{33},\dot{\rho}_{44}\approx 0$, the density matrix elements $\rho_{13},\rho_{23},\rho_{14},\rho_{24}$ read in terms of ρ_{11},ρ_{22} and ρ_{12} as follows

$$
\begin{aligned}
\rho_{13} &= \frac{1}{\Delta_s + \alpha_p t}\Omega_{p0}(t)\rho_{11} + \frac{1}{\Delta_s + \alpha_p t}\Omega_{s0}(t)\rho_{12} \\
\rho_{23} &= \frac{1}{\Delta_s + \alpha_s t}\Omega_{s0}(t)\rho_{22} + \frac{1}{\Delta_s + \alpha_s t}\Omega_{p0}(t)\rho_{21} \\
\rho_{14} &= \frac{1}{\Delta_{as}}\Omega_{as0}(t)\rho_{11} + \frac{1}{\Delta_{as}}\Omega_{pr0}(t)\rho_{12} \\
\rho_{24} &= \frac{1}{\Delta_{as} + \alpha_{as} t}\Omega_{pr0}(t)\rho_{22} + \frac{1}{\Delta_{as} + \alpha_{as} t}\Omega_{as0}(t)\rho_{21}
\end{aligned}
\tag{19}
$$

Substituting Eq.(19) in Eq.(18) provides the Maxwell's equations for four components of the field as a function of coherence ρ_{12} between states $|1>$ and $|2>$

$$
\begin{aligned}
\frac{1}{c}\frac{\partial E_p}{\partial t} = \frac{\partial E_p}{\partial z} \quad &= -\frac{\eta N_A \mu_0}{2(\Delta_s + \alpha_p t)}\mu_{13} c\omega_p \Omega_{s0}(t)\,\mathrm{Im}[\rho_{12}] \\
\frac{1}{c}\frac{\partial E_s}{\partial t} = \frac{\partial E_s}{\partial z} \quad &= \frac{\eta N_A \mu_0}{2(\Delta_s + \alpha_s t)}\mu_{23} c\omega_s \Omega_{p0}(t)\,\mathrm{Im}[\rho_{12}] \\
\frac{1}{c}\frac{\partial E_{pr}}{\partial t} = \frac{\partial E_{pr}}{\partial z} \quad &= \frac{\eta N_A \mu_0}{2(\Delta_{as} + \alpha_{as} t)}\mu_{24} c\omega_{as} \Omega_{as0}(t)\,\mathrm{Im}[\rho_{12}] \\
\frac{1}{c}\frac{\partial E_{as}}{\partial t} = \frac{\partial E_{as}}{\partial z} \quad &= -\frac{\eta N_A \mu_0}{2(\Delta_{as})}\mu_{14} c\omega_{pr} \Omega_{pr0}(t)\,\mathrm{Im}[\rho_{12}]
\end{aligned}
\tag{20}
$$

These equations, coupled with the multi-layer model described below, are numerically solved using transform limited and control pulse trains to find the scattered anti-Stokes signal.

To analyze the impact of decoherence due to spontaneous decay and collisional dephasing of molecules, the Liouville von Neumann equations are augmented by the relaxation terms. The CARS scheme is considered to be two coinciding Λ-systems. Spontaneous decay from state $|i\rangle$ to state $|j\rangle$ is denoted by γ_{ij}, while collisional dephasing between states $|i\rangle$ and $|j\rangle$ is denoted by Γ_{ij}.

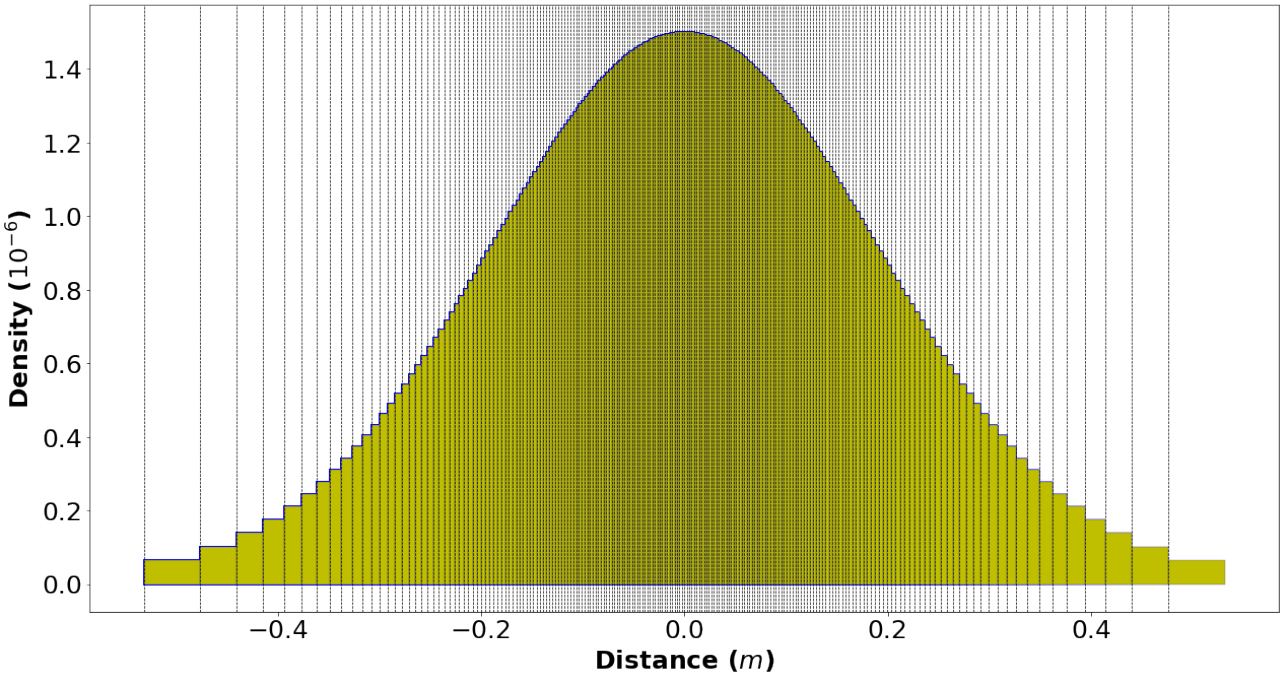

FIG. 3: An example of the multi-layer model of a molecular distribution for the width of the Gaussian distribution in Eq.(23) of the target molecules $\sigma = 0.19$ m. Here, each of 200 vertical lines represents the location of the scattering event and the scattering layers become more dense as the density peaks at the center.

$$
\begin{aligned}
\dot{\rho}_{11} &= -i/\hbar[H, \rho_{11}] + \gamma_{31}\rho_{33} + \gamma_{41}\rho_{44} \\
\dot{\rho}_{12} &= -i/\hbar[H, \rho_{12}] + \Gamma_{21}\rho_{12} \\
\dot{\rho}_{13} &= -i/\hbar[H, \rho_{13}] - (\gamma_{31}/2 + \gamma_{32}/2 + \Gamma_{31})\rho_{13} \\
\dot{\rho}_{14} &= -i/\hbar[H, \rho_{14}] - (\gamma_{41}/2 + \gamma_{42}/2 + \Gamma_{41})\rho_{14} \\
\dot{\rho}_{22} &= -i/\hbar[H, \rho_{22}] + \gamma_{32}\rho_{33} + \gamma_{42}\rho_{44} \\
\dot{\rho}_{23} &= -i/\hbar[H, \rho_{23}] - (\gamma_{31}/2 + \gamma_{32}/2 + \Gamma_{32})\rho_{23} \\
\dot{\rho}_{24} &= -i/\hbar[H, \rho_{24}] - (\gamma_{41}/2 + \gamma_{42}/2 + \Gamma_{42})\rho_{24} \\
\dot{\rho}_{33} &= -i/\hbar[H, \rho_{33}] - (\gamma_{31} + \gamma_{32})\rho_{33} \\
\dot{\rho}_{34} &= -i/\hbar[H, \rho_{34}] + \Gamma_{43}\rho_{34} \\
\dot{\rho}_{44} &= -i/\hbar[H, \rho_{44}] - (\gamma_{41} + \gamma_{42})\rho_{44}.
\end{aligned}
\tag{21}
$$

In numerical analyses, parameters γ_{ij} are all the same and equal to γ, $\Gamma_{21} = \Gamma_{43} = 0$ because respective pairs of states assumed to loose coherence at the same rate, while the

rest Γ_{ij}'s are the same and equal to Γ.

B. The target molecules distribution

We consider the target molecules as a cluster of molecules with its center located a large distance away from the source and its density following the Gaussian distribution. We introduce a layer model to analyze the propagation and scattering of the pump, the Stokes, the probe and the anti-Stokes pulses through this distribution. In the layer model, each layer is characterized by the fractional number density η and a distance to it adjacent layer $(\Delta z)_\eta$. The distance between the layers changes according to the Gaussian distribution of molecules. If N_s is the number of the target molecules and N is the number of total molecules associated with the layer, the fractional number density of that layer is defined as $\eta = N_s/N$. Suppose all target molecules in the layer are arranged vertically next to each other with no background molecules between them, then the area occupied by these molecules $S = \pi(d/2)^2 N_s$ giving $N_s = 4S/\pi d^2$, where d is an approximate diameter of the target molecule. If $(\Delta z)_\eta$ is the width of this layer, the total number of molecules N is $(S(\Delta z)_\eta/V_0)N_A$. This gives

$$\eta = \frac{N_s}{N} = \frac{\frac{4S}{\pi d^2}}{(\frac{S(\Delta z)_\eta}{V_0})N_A} = \frac{4V_0}{\pi d^2 (\Delta z)_\eta N_A}, \tag{22}$$

where V_0 is the molar volume. Consider that the density changes as per the Gaussian distribution function with its maximum value at the center z_0 of the cluster of molecules as

$$\eta = \frac{N_s V_0}{S N_A \sqrt{2\pi}\sigma} e^{-(z-z_0)^2/(2\sigma^2)}. \tag{23}$$

The maximum density η_{max}, which is the density of the central layer, is found by substituting $z = z_0$ in Eq.(23). This value of η is then substituted in the Eq.(22) to find the width of the central layer $(\Delta z)_\eta$. Once we find the width of the central layer, the η of the adjacent layer is found by substituting the new value of z, $z_0 + (\Delta z)_\eta$, in Eq.(23). This process is repeated to find the entire density distribution of the cluster of molecules. The distance between scattering layers $(\Delta z)_\eta$ increases towards both ends of the distribution. So we converted the three dimensional cluster of molecules into a set of two-dimensional layers of molecules. Fig.(3) shows a set of layers, the distance between them and the density

associated with each layer. In numerical calculations, we consider $\sigma = 1m$ with its center 1 km away from the source, which together with η_{max} determines the total number of layers to be equal to 346.

C. Propagation through atmosphere

For a completeness of the picture, the propagation of pulses through the atmosphere as they reach the molecular distribution needs to be taken into account. The propagation of femtosecond pulses through the atmosphere under various air conditions has been broadly investigated, e.g. [28, 29]. Various effects during the propagation including the dispersion and the nonlinear self-focusing are not within the scope of this paper. We use Beer's law under the ideal conditions to account for the change in the amplitude of the pulses as they propagate through the atmosphere [30]. Assuming there is no turbulence and the air is homogeneous, the intensity of the pulse trains attenuates exponentially due to scattering and absorption as they propagate. The intensity I as a function of the distance z can be written as: $I(z) = I_0 e^{-\beta_e z}$, where β_e is the extinction coefficient that contains factors of both scattering and absorption. We use the clear air atmospheric coefficient of 0.55 km^{-1} in numerical calculations [31]. Numerical analysis shows that the amplitude of the pump, the Stokes and the probe pulse trains is reduced upon propagation, while the average intensity of the anti-Stokes pulse trains is amplified as shown in Fig.(4) for propagation through 200 layers for both cases, with and without impact from the air. The intensity of the anti-Stokes pulse trains in the presence of the air is depreciated due to the scattering and absorption effects.

IV. DEEP NEURAL NETWORKS FOR EVALUATION OF THE PHASE OF THE FIELDS SCATTERED FROM THE TARGET MOLECULES

We use a machine learning model for the analysis of the numerical values of the phase of the electromagnetic fields in the numerical code for propagation of the Maxwell - Liouville von Neumann equations [32, 33]. The main function of the model is to get the analytical phase from the numerical values of the pulse. This is extremely important measure in order to accurately evaluate the phase of the fields modifying after each scattering event with the

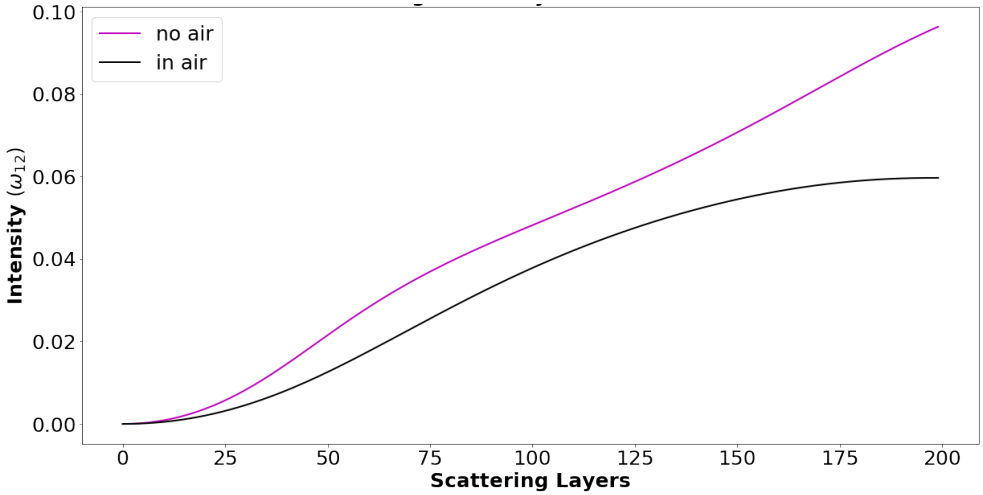

FIG. 4: An average intensity of the anti-Stokes pulses as a function of the number of scattering layers calculated using Beer's law. The curves represent the change in average intensity as pulses undergo scattering through layers for the case of $\beta_e = 0$ (without taking air into consideration), and for $\beta_e = 0.55\ km^{-1}$. The depreciation of intensity in the second case is due to scattering and absorption in the air.

target molecules. The machine learning model is the deep convolution neural networks. It classifies the kind of the phase of the pulse, which may have three different chirps: linear, quadratic and the chirp shape according to our control scheme $\alpha_s = -\alpha_p$ and $\alpha_{pr} = \alpha_s - \alpha_p$ for $t \leq t_c$; and $\alpha_s = \alpha_p$ and $\alpha_{pr} = 0$ for $t > t_c$.

Of principle importance for studying the phase of the numerical pulses is the availability of training data. Massive training data is a necessary requirement for deep learning training to concur a problem [34]. Since it is difficult to collect thousands of actual data from the experiments, we created a program that generated the scattered laser pulses randomly based on an arbitrary laser pulse model

$$E(t) = E_0 e^{-\frac{t^2}{2\tau^2}} \cos[\omega_L t + M(t)]. \tag{24}$$

Here τ is a single pulse duration, E_0 is the peak value of the field having the Gaussian envelope, and $\omega_L t + M(t)$ is the phase of the field having the modulation $M(t)$, which is the key to quantum control. A different parity of the phase modulation leads to different control scenarios [35, 36]. Here we present $M(t)$ as an expansion in the Taylor series

$$M(t) = a_0 + a_1 t^1 + a_2 t^2 + a_3 t^3 + ... \tag{25}$$

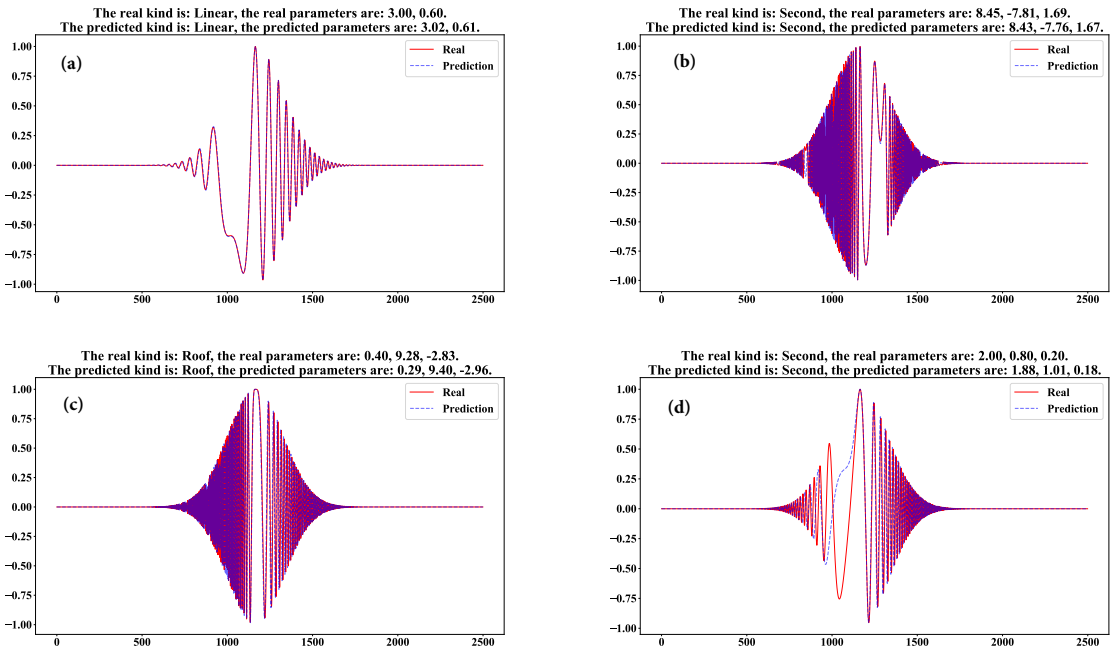

FIG. 5: Different shapes of the phase of the field obtained numerically (solid line) and using the deep convolution neural networks model (dashed line) with different types of the phase of the input pulse: (a) Linear chirp, $\phi(t) = a_1 t + a_2 t^2$; (b) Quadratic dependence of the phase on time having $a_2 < 0$ in $\phi(t) = a_1 t + a_2 t^2 + a_3 t^3$; (c) 'Roof' chirp having positive chirp rate for the first and negative chirp rate for the second part of the pulse [3], $\phi(t) = a_1 t + \tilde{a}_2 t^2$ for $t \leq 0$, and $\phi(t) = a_1 t + \widetilde{\tilde{a}}_2 t^2$ for $t > 0$; (d) Quadratic dependence of the phase on time having $a_2 > 0$ in $\phi(t) = a_1 t + a_2 t^2 + a_3 t^3$. The values of parameters are printed in the titles of the pictures. Note that there is no discrepancy in determination of the kind of the phase, only parameters have rare errors.

Since in most cases the higher orders have a very limited contribution, we created data for three kinds of the phase using terms up to the third power in time: 'The Linear,' which is determined by two parameters: the carrier frequency (a_1) and the linear chirp (a_2), then the field phase reads $\phi(t) = a_1 t + a_2 t^2$; 'The Second', which is determined by three parameters: the carrier frequency (a_1), the linear chirp (a_2), and the second order chirp (a_3), then the phase reads $\phi(t) = a_1 t + a_2 t^2 + a_3 t^3$; and 'The Roof', which is comprised of two parts, before central time and after, and is determined by three parameters: the carrier frequency (a_1), the linear chirp ($\tilde{a}_2$) for the first half of the pulse and the linear chirp ($\widetilde{\tilde{a}}_2$) for the second half of the pulse, then the constructed phase of the field reads $\phi(t) = a_1 t + \tilde{a}_2 t^2$ for $t \leq 0$,

and $\phi(t) = a_1 t + \widetilde{\widetilde{a}}_2 t^2$ for $t > 0$.

We simulated the pulses with these three kinds of phases using characteristic values of the field parameters and generated training data in quantity of 50,000 for each kind by varying the carrier frequency and the chirp rate. During the training process, we applied the Adam Optimizer algorithm with the learning rate of 0.1, and the regularization of 0.02 [37]. The loss function of the classifier model is the cross entropy, but the mean squared error for the regression model. The early stop technique was also used to control the overfitting [38].

Regarding the construction of the neural networks for both the classification and the regression models - they share the same core structure. Since the numerical pulses, which we generated as the training data, have 2500 time steps, all models have the input shape of 2500×1. There are three blocks of mini-convolutional neural networks in the models. The first block contains three 1D convolutional layers with the kernel size of 3. The second block has two layers of the 1D convolutional networks with kernel size of 5. The third block has a single 1D convolutional layer of kernel of 7. All the convolutional layers are activated by the Rectified Linear Units Function [39] and the Group Normalization [40]. There is a maximum pooling layer of pool size 4 after each block. There is a linear layer of size 1024 after the output of the convolutional blocks is flattened. Such a structure is chosen to satisfy the requirements for extracting the instantaneous parameters from the sub-regions of the original input tensor.

After training the classification and the regression models, they are combined to be used as directed. The classification block classifies the random pulse and sends it to the corresponding regression block to solve for the analytical parameters of one of three kinds of the phase. The classification reaches the accuracy of 97.93%, and the overall root mean square error of the regression is smaller than 0.1, providing the deep learning model's results accurate enough. To demonstrate high accuracy of the analytical fit to the numerical data of the phase of the field we show several prototypical phases in Fig.(5).

V. NUMERICAL RESULTS

Numerical analyses of the effects of the pulse shaping on the optimization of quantum coherence and mitigation of decoherence in the target molecules as well as the impact of multiple scattering from the target molecules are performed using the methanol molecule

having the Raman active symmetric stretch mode at 2837 cm^{-1} (85.05 THz) [15]. First we investigate the dependence of the population and coherence on the peak Rabi frequency of the transform-limited pulses and control pulses and reveal adiabatic type of solution leading to the maximum vibrational coherence for the latter. Then we analyze the four-level system dynamics subject to the interaction with the control pulse trains in the presence of decoherence and demonstrate a sustainable value of vibrational coherence. Finally, we show the solution of the Maxwell - Liouville von Neumann equations for the control pulse trains interacting with an ensemble of methanol molecules illustrating growth of the vibrational coherence and the anti-Stokes component of the propagating fields.

Fig.(6(a)-(d)) shows the dependence of the populations and coherence as a function of the peak Rabi frequency for the case of the transform-limited pump, Stokes and probe pulses with zero and non-zero one-photon detuning (a),(b), and control pulses with zero and non-zero one-photon detuning (c),(d) respectively. The envelope of the Rabi frequency is the same for all three transform-limited pulses, which are also used as an initial condition for chirping in the control scheme. Under the one-photon resonance condition shown for the transform-limited pulses in (a) and for the chirped pulses in (b), the population of the excited states is significant, which prevents from achieving an equal population between the ground state $|1\rangle$ and the excited vibronic state $|2\rangle$. In the transform-limited pulse scenario in (a), coherence never exceeds the value 0.4 and periodically becomes zero, which is not the case for the control pulses solution shown in (b). Such behavior in (a) is due to the pulse area type of solution, when the probability amplitude of the states depends on the pulse area with π value leading to the population inversion and 2π - to the population return. In contrast, the control pulse scheme provides adiabatic type of response in the four-level system with coherence changing within a range between 0.2 and 0.45 depending on the strength of the fields as shown in (b). The one-photon detuning $\Delta_s = \Delta_{as} = \Delta = 1.0[\omega_{21}]$ minimizes the transitional population of the excited states $|3\rangle$ and $|4\rangle$ for both transform-limited and the control pulse scenario shown in (c) and (d) respectively. The one-photon detuning shifts the point of first zero coherence toward higher values of the Rabi frequencies in the transform-limited case in (c). In the control case in (d), the point of equal population giving the maximum vibrational coherence occurs at the peak Rabi frequency $\Omega_{p0} = 0.82[\omega_{21}]$ and is achieved due to two-photon adiabatic passage with a negligible involvement of the excited state manifold into population dynamics. Beyond this point, coherence value varies within

the range from 0.5 to 0.2. Once coherence is built, it never drops to zero, in contrast to the transform-limited pulses solution. Thus, the detuned chirped pulse control scheme is more robust for the applications in CARS microscopy and spectroscopy because it provides one with a sustainable value of coherence resilient to fluctuations in the intensity of the Raman fields. To demonstrate adiabatic passage generated under the condition of nonzero one-photon detuning, a time-dependent picture is presented in Fig.(7(a),(b)). The time dependence of the population and coherence in the four level system interacting with the transform-limited pump, Stokes and probe pulses, (a), and with the control pulses (b) shows adiabatic population transfer from the ground state $|1\rangle$ to the excited vibronic state $|2\rangle$. The value of the Rabi frequency $\Omega_{p0} = 0.82[\omega_{21}]$ is chosen according to the Fig.(6(d)), which generates equal population between the ground state $|1\rangle$ and the excited state $|2\rangle$ and the maximum coherence ρ_{21} in the control pulses scenario. Meanwhile, the transform-limited pulses induce unequal population distribution between state $|1\rangle$ and state $|2\rangle$ lowering coherence. In Fig.(7(a),(b)), spontaneous decay rate $\gamma = 1THz$ does not make any visible contribution to the population dynamics within a single pulse duration. However, when the four-level system interacts with the control pulse trains each consisting of ten pulses, having the pulse train period the same as decay time $T = 1/\gamma = 1ps$, spontaneous decay increases population of states $|1\rangle$ (dashed red) and $|2\rangle$ (dotted black) by decreasing the population of states $|3\rangle$ (dash-dotted green) and $|4\rangle$ (solid yellow), shown in Fig.(8(a)), and thus, slightly changing the value of coherence ρ_{21} (solid black). Switching on collisional dephasing ($\Gamma = \gamma = 1THz$) reduces coherence in the system more dramatically as it is shown in Fig.(8(b)). However coherence does not drop to zero between pulses. This is due to the choice of the pulse repetition rate as well as the control scheme leading to a negligible population of the excited states $|3\rangle$ and $|4\rangle$ in the dynamics. Notably, control pulse trains keep population inversion between states $|1\rangle$ and $|2\rangle$.

Using Maxwell's equations Eqs.(20) coupled to the Liouville von Neumann equations Eqs. (19) we numerically analyzed the propagation effects of the pump, the Stokes, the probe and the anti-Stokes fields scattered from the target molecules and observed the amplification of the anti-Stokes component. The machine learning approach was implemented to reveal the modulation of the phase of four field components after each scattering. Fig.(9) shows the control pump, Stokes, probe and the built-up anti-Stokes pulses after each of five consecutive scattering events for the parameters of the fields $\Omega_{p(s,pr)} = 85THz$ ($E_{p(s,pr)_0} \sim 1.6\times10^9 V/m$),

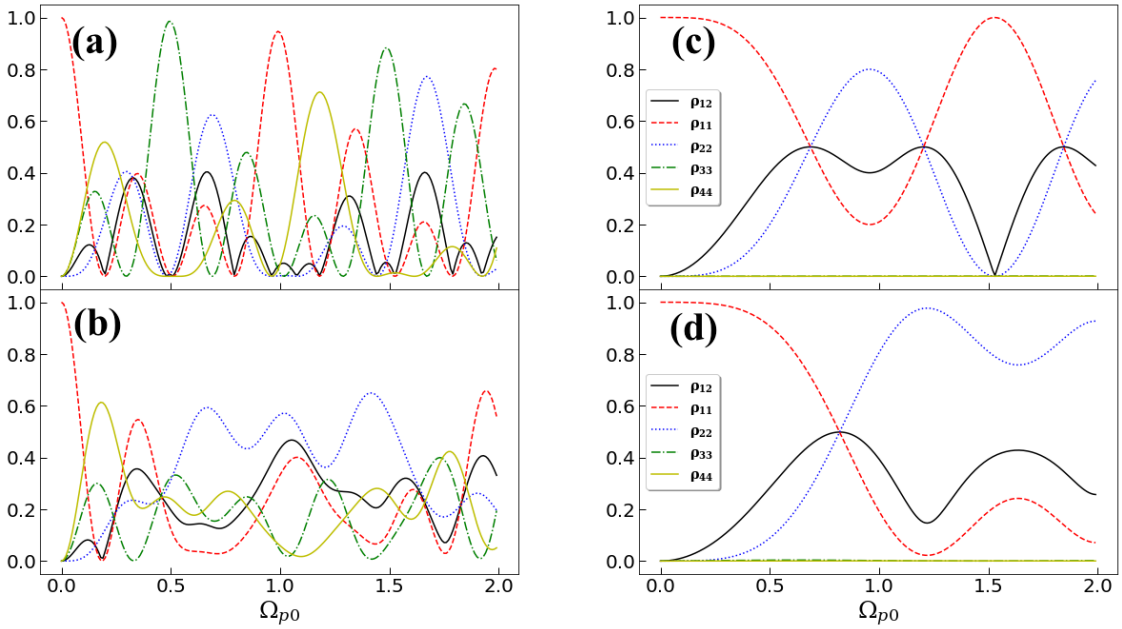

FIG. 6: The population and coherence in the four-level system as a function of the peak Rabi frequency $\Omega_p[\omega_{21}]$, which is the same for the pump, the Stokes and the probe pulses, $\omega_{21} = 85$ THz. Parameters used in the calculations are $\tau_0 = 4.66[\omega_{21}^{-1}], \Gamma = \gamma = 0$. In (a) the transform-limited pump, Stokes and probe pulses with zero one-photon detuning are applied, $\Delta_s = \Delta_{as} = \Delta = 0$; (b) the control pump, Stokes and probe pulses with zero one-photon detuning are applied $\alpha_s'/\tau_0^2 = -1.0, \Delta = 0$; (c) the transform-limited pulses with non-zero one-photon detuning are applied, $\Delta = 1.0[\omega_{21}]$; (d) Control pulses with non-zero one-photon detuning are applied, $\alpha_s'/\tau_0^2 = -1.0, \Delta = 1.0[\omega_{21}]$. Once coherence is built by the control pulses, it never drops to zero, in contrast to the transform-limited pulses solution. The detuned control scenario is even more robust for the applications in CARS microscopy and spectroscopy because it provides sustainable value of coherence resilient to fluctuations in the intensity of the Raman fields.

$\tau_0 = 100fs$, $\alpha_s = 7THz/fs$, $\Delta_s = \Delta_{as} = \Delta = 85THz$ and $\Gamma = \gamma = 1THz$. The anti-Stokes component is built up having the peak Rabi frequency about $10^{-8}\Omega_p$ after the fifth iteration, which is about $\sim 16V/m$.

We also analyzed propagation effects using the transform-limited pump, Stokes, and probe pulse trains having the peak Rabi frequency $\Omega_{p(s,pr)} = 85THz = \omega_{21}$ and been largely

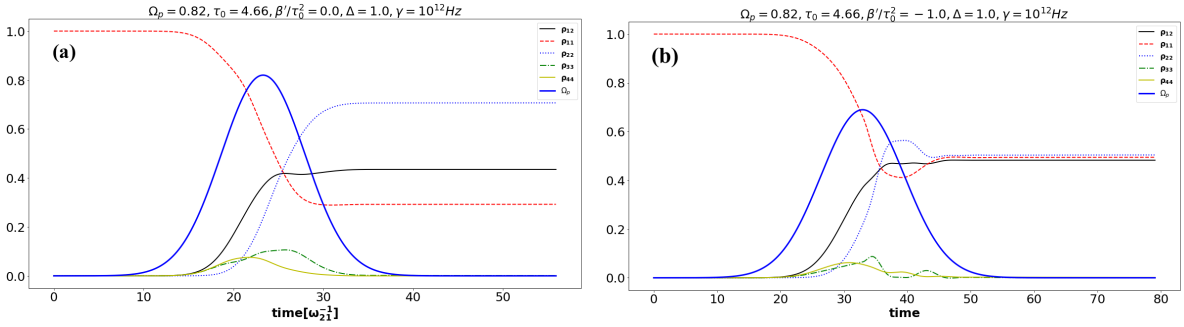

FIG. 7: Dynamics of the population of four states ρ_{11} (dashed red), ρ_{22} (dotted black), ρ_{33} (dash-dotted green), ρ_{44} (solid brown) and coherence ρ_{21} (solid black) in the four-level system interacting with (a) the transform-limited pump, Stokes and probe pulses; (b) the control pulses, $\alpha_s'/\tau_0^2 = -1.0$. Other parameters are the peak Rabi frequency of the pump, the Stokes and the probe pulses before chirping

$$\Omega_p = 0.82[\omega_{21}], \tau_0 = 4.66[\omega_{21}^{-1}], \gamma = 1.176 \times 10^{-2}[\omega_{21}], \Gamma = 0, \Delta = 1.0[\omega_{21}].$$

detuned from the one-photon transitions, the detuning is $\Delta_s = \Delta_{as} = \Delta = 10\omega_{21} = 850THz$ for the adiabatic regime. We consider 10 pulses in the pulse train having period $T = 1ps$ equal to decoherence time $1/\Gamma = 1/\gamma = 1ps$. The increase of the peak value of the anti-Stokes Rabi frequency $\Omega_{as}(t)$ by three orders of magnitude is observed 3.5 meters (699 layers) away from the peak molecular density. Coherence is increasing from pulse to pulse and the population is adiabatically transferred from the ground state $|1\rangle$ to the excited state $|2\rangle$ in the four-level system during the interaction with four fields in the CARS configuration. Here adiabatic regime is achieved due to a large one-photon detuning $\Delta = 10\omega_{21}$ and the choice of the peak Rabi frequency $\Omega_{p(s,pr)} = \omega_{21}$, which result in a negligible population of the transitional states $|3\rangle$ and $|4\rangle$. In combination with the choice of the pulse train period, which is the same as the relaxation time $T = 1/\Gamma = 1/\gamma$, decoherence is efficiently mitigated in such a system.

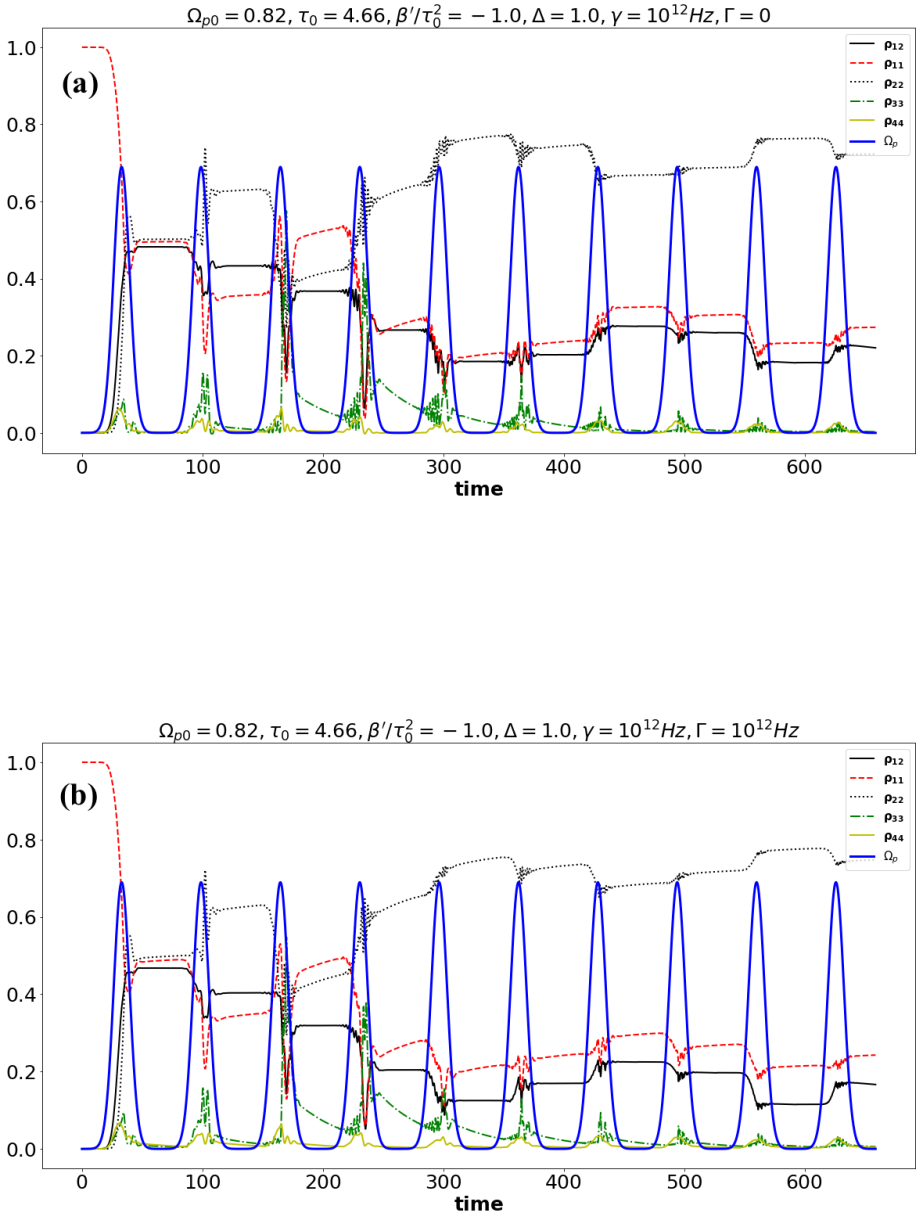

FIG. 8: Dynamics of the population of four states ρ_{11} (dashed red), ρ_{22} (dotted black), ρ_{33} (dash-dotted green), ρ_{44} (solid brown) and coherence ρ_{21} (solid black) in the four-level system interacting with the control pulse trains having the repetition rate equal to the spontaneous decay rate of 1 THz and (a) zero collisional dephasing rate, and (b) collisional dephasing rate of 1 THz. Other parameters are $\alpha_s'/\tau_0^2 = -1.0$, $\Omega_{p_0} = 0.82[\omega_{21}]$, (the peak Rabi frequency of the pump, the Stokes and the probe pulses before chirping), $\tau_0 = 4.66[\omega_{21}^{-1}], \Delta_s = \Delta_{as} = \Delta = 1.0[\omega_{21}]$. The vibronic state $|2\rangle$ is maintaining higher population than the ground state $|1\rangle$ giving coherence value within 0.1-0.4 range.

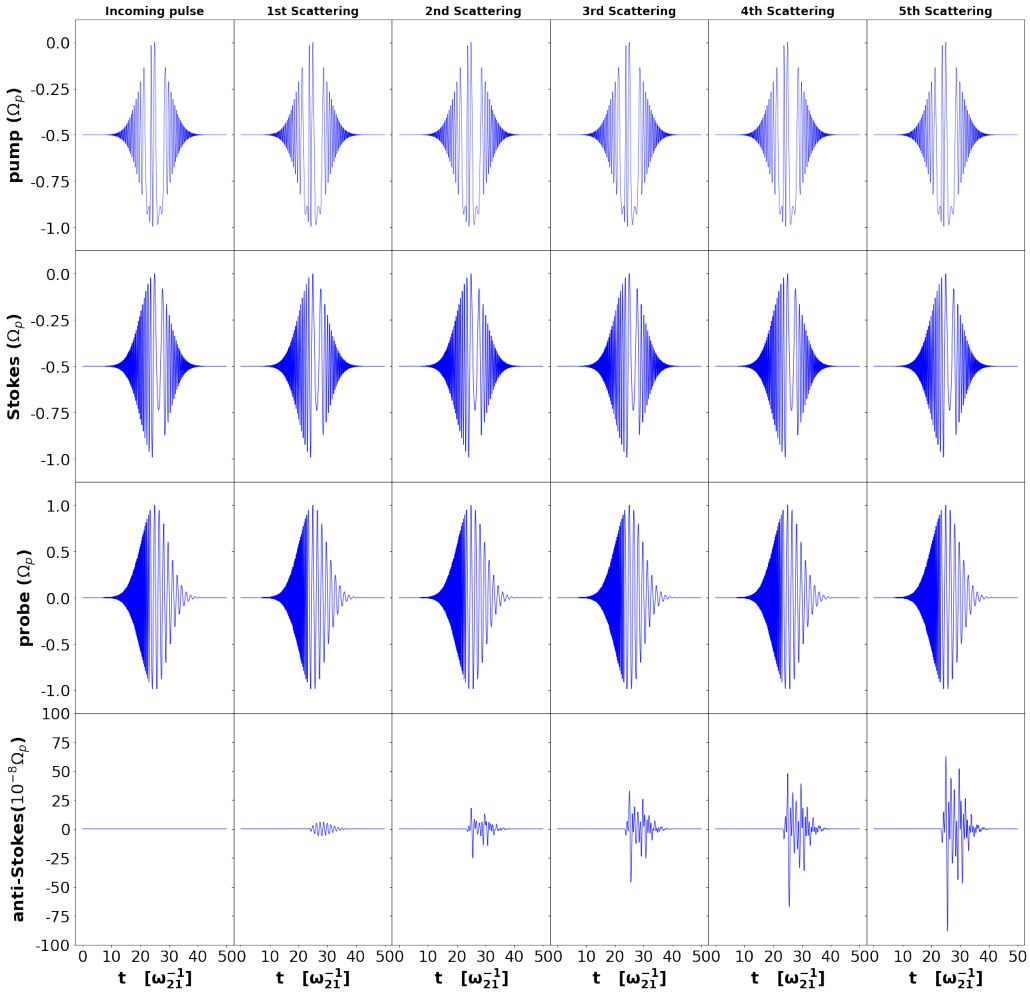

FIG. 9: The pump, the Stokes, the probe and the built-up anti-Stokes chirped pulses after each of five consecutive scattering events. The incident pump, the Stokes and the probe pulses are chirped in accordance with the control scheme: For the first half of the pulse duration, $t \leq t_c$, $\alpha_s = -\alpha_p$, where α_p is the chirp of the pump pulse, α_s is the chirp of the Stokes pulse, and the chirp rate of the probe pulse is $\alpha_{pr} = \alpha_s - \alpha_p$; and for the second half of the pulse duration, $t > t_c$, $\alpha_s = \alpha_p$ and $\alpha_{pr} = 0$. The Stokes pulse chirp rate is $\alpha_s = 7THz/fs$ and the pulse duration of three pulses is the same, $\tau_0 = 100fs$. The anti-Stokes field is built up gradually and constitutes $\sim 10^{-8}$ of the amplitude of the incident field.

VI. OUTCOME

From the results above it follows that the implementation of the control pulse trains in the four-wave mixing in CARS is more robust for the generation of a sustainable anti-Stokes

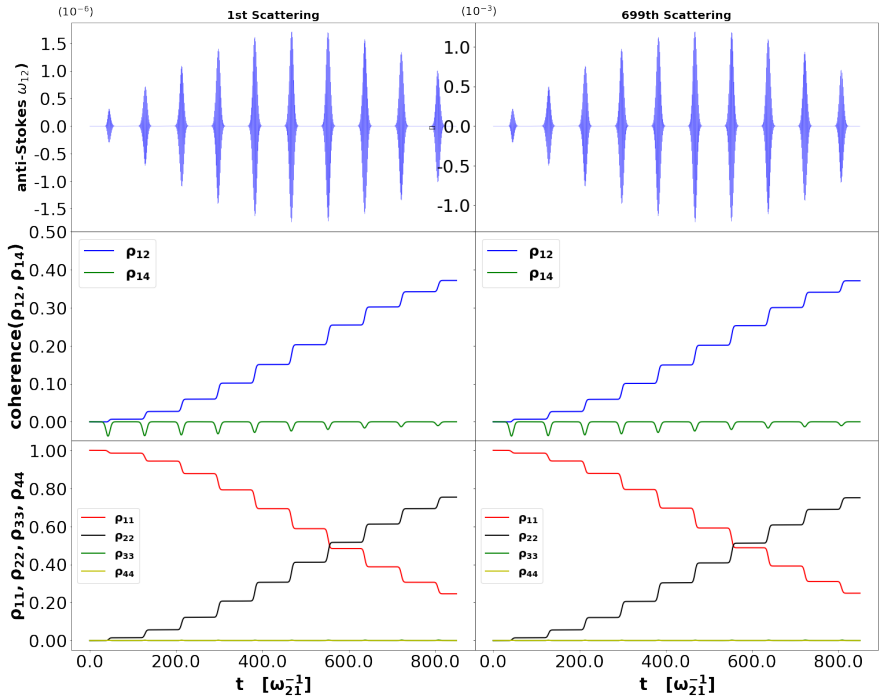

FIG. 10: Scattering dynamics using the transform-limited pump, Stokes, and probe pulse trains having the peak Rabi frequency equal to the frequency between states $|1\rangle$ and $|2\rangle$, $\Omega_{p(s,pr)_0} = \omega_{21}$, and been largely detuned from the one-photon transitions, the detuning is $\Delta_s = \Delta_{as} = \Delta = 10\omega_{21} = 850THz$ for adiabatic regime. There are 10 pulses in each pulse train. The first raw shows ten anti-Stokes pulses (top), the state coherence (middle) and populations (bottom) after the first scattering event; the second raw shows the same after the 699th scattering event. Parameters $\sigma = 1m$; 699 layers provide a distance of 3.5 m away from the peak molecular density; $\tau_0 = 100fs$; $T = 1ps$; $1/\Gamma = 1/\gamma = 1ps$. The peak amplitude of the pulse trains is reduced as a result of transferring the energy to the anti-Stokes component in the process. The amplitude of the anti-Stokes pulses is increased after each scattering, giving a significant amplification of the peak Rabi frequency $\Omega_{as}(t)$ after the 699th scattering, from $10^{-6}[\omega_{21}]$ generated during the 1st scattering to $10^{-3}[\omega_{21}]$ after 699th scattering event.

backscattered signal compared to the use of a set of transform-limited pulses. This is due to the adiabatic regime of light-matter interaction which preserves vibrational coherence and facilitates a built-up of the anti-Stokes signal. For the case of the phase-matching conditions relaxed, given the size of the molecules is less than the wavelength of the incident fields, a collinear copropagating configuration of CARS may be created using the methanol as a

surrogate target. Because the anti-Stokes radiation is generated as a result of the stimulated Raman scattering process, it is highly directional and is built up in the forward and the backward directions dominantly [4, 19]. Therefore, the backscattered anti-Stokes signal will reach a detector near the laser source. Importantly, our quantum control method optimizes the macroscopic induced polarization in the target molecules by maximizing vibrational coherence. This results in the enhancement of the anti-Stokes signal in the backward direction. The mechanism is through chirping of the incident pulse trains, which induces adiabatic population transfer within four states in the CARS scheme and leads to a sustainable, high vibrational coherence. Note, that the transitional excited states are negligibly populated, thus the impact of spontaneous decay and associated losses of coherence are minimal. Under these conditions, decoherence is significantly reduced, which is a foundation for the propagation of the anti-Stokes signal through distances on a kilometer scale. The following parameters of the fields may be used in an experiment: the pulse duration of order $100fs$, the peak field amplitude of $E_{0p(s,pr)} \sim 1.6 \times 10^9 V/m$; the control pulse chirps obeying the relationship $\alpha_s = -\alpha_p$, and $\alpha_{pr} = \alpha_s - \alpha_p$ for the first half of the pulse duration $t \leq t_c$, and $\alpha_s = \alpha_p$, $\alpha_{pr} = 0$ for $t > t_c$; the value of $\alpha_s = 7THz/fs$, the pulse train period of order of spontaneous decay time and the one-photon detuning of order $\Delta \sim 1/fs$.

---

[1] Jabir Chathanathil, Dmitry Budker, Svetlana A. Malinovskaya, "Quantum control via chirped coherent anti-Stokes Raman spectroscopy," Quantum Sci. Technol., accepted (2023).

[2] J. Chathanathil, G. Lui, S. A. Malinovskaya, "A semi-classical control theory of Coherent Anti-Stokes Raman Scattering (CARS) maximizing vibrational coherence for remote detection," Phys. Rev. A, **104,** 043701 (15pp) (2021).

[3] N. Pandya, G. Lui, F. A. Narducci, J. Chathanathil, S. A. Malinovskaya, "Creation of the maximum coherence via adiabatic passage in the four-wave mixing process of coherent anti-Stokes Raman scattering," Chem. Phys. Lett., **738,** 136763 (5pp) (2020).

[4] Gengyuan Liu, Frank A. Narducci, Svetlana A. Malinovskaya, "Limits to remote molecular detection via coherent anti-Stokes Raman spectroscopy using a maximal coherence control technique," J. Mod. Opt. **67,** 21-25 (2020).

[5] J. Chathanathil, S. A. Malinovskaya, "Chirped pulse control of Raman coherence in atoms

and molecules," Advances in Quant. Chem. **89** (2023) in production.

[6] Ramaswamy, A., Malinovskaya, S.A. (2022). Control with EIT: High Energy Charged Particle Detection. In: Ünlü, H., Horing, N.J.M. (eds) Progress in Nanoscale and Low-Dimensional Materials and Devices. Topics in Applied Physics, vol 144. (33pp) Springer, Cham. https://doi.org/10.1007/978-3-030-93460-6_12.

[7] I. R. Sola, B. Y. Chang, S. A. Malinovskaya, S. C. Carrasco, V. S. Malinovsky, "Stimulated Raman adiabatic passage with trains of weak pulses," J. Phys. B: At. Mol. Opt. Phys. **55**, 234002 (15pp) (2022).

[8] A. Ramaswamy, A.F. Latypov, S.A. Malinovskaya, "Generation of the GHZ and the W state in a series of Rydberg atoms trapped in optical lattices," Adv. Theo. Comp. Phys. **5(3)**, 476-484 (2022).

[9] Elliot Pachniak, Svetlana A. Malinovskaya, "Creation of quantum entangled states of Rydberg atoms via chirped adiabatic passage," Nature Sc. Rep. **11,** 12980 (9pp) (2021).

[10] Svetlana A. Malinovskaya, "Laser cooling using adiabatic rapid passage," Frontiers of Phys. **16,** 52601 (1p) (2021).

[11] *Coherent Raman Scattering Microscopy,* Eds: J.-X. Cheng, X. S. Xie, Taylor & Francis Group, LLC (2013).

[12] M. Dantus, R.M. Bowman, A.H. Zewail, "Femtosecond laser observations of molecular vibration and rotation," Nature, **343,** 737 (1990).

[13] S.A. Malinovskaya, "Observation and control of molecular motion using ultrafast laser pulses," In: Trends in Chemical Physics Research, Editor: A.N. Linke, Nova Science Publishers, Inc. ISBN 1-59454-483-2, pp. 257-280 (2005).

[14] S.A. Malinovskaya, "Chirped pulse control methods for imaging of biological structure and dynamics," I.J. Quant. Chem., **107,** 3151 (2007).

[15] S. A. Malinovskaya, "Mode selective excitation using ultrafast chirped laser pulses", Phys. Rev. A. **73,** 033416 (2006).

[16] M.O. Scully, M.S. Zubairy, *Quantum Optics,* Cambridge University Press (1997).

[17] M. O. Scully, G. W. Kattawar, R. P. Lucht, T. Opatrny, H. Pilloff, A. Rebane, A. V. Sokolov, M. S. Zubairy, "FAST CARS: Engineering a laser spectroscopic technique for rapid identification of bacterial spores," P. Natl. Acad. Sci. USA **99,** 10994 (2002).

[18] D. Pestov, R. K. Murawski, G. O. Ariunbold, X. Wang, M. C. Zhi, A. V. Sokolov, V. A.

Sautenkov, Y. V. Rostovtsev, A. Dogariu, Y. Huang, M. O. Scully, "Optimizing the laser-pulse configuration for coherent Raman spectroscopy," Science **316,** 265 (2007).

[19] C.H.R. Ooi, G. Beadie, G. Kattawar, J.F. Reinjes, Y. Rostovtsev, M.S. Zubairy, M.O. Scully, "Theory of femtosecond coherent anti-Stokes Raman backscattering enhanced by quantum coherence for standoff detection of bacterial spores", Phys. Rev. A, **72**, 023807 (2005).

[20] D. Oron, N. Dudovich, D. Yelin, Y. Silberberg, "Narrow-band coherent anti-Stokes Raman signals from broad-band pulses," Phys. Rev. Lett. **88,** 063004 (2002).

[21] D. Oron, N. Dudovich, Y. Silberberg, "Femtosecond phase-and-polarization control for background-free coherent anti-Stokes Raman spectroscopy," Phys. Rev. Lett. **90,** 213902 (2003).

[22] V. V. Lozovoy, B. W. Xu, J. C. Shane, M. Dantus, "Selective nonlinear optical excitation with pulses shaped by pseudorandom Galois fields," Phys. Rev. A **74,** 041805(R) (2006).

[23] H. Li, D.A. Harris, B. Xu, P.J. Wrzesinski, V.V. Lozovoy, M. Dantus, "Coherent mode-selective Raman excitation towards standoff detection," Opt. Expr. **16,** 5499 (2008).

[24] R. M. Onorato, N. Muraki, K. P. Knutsen, R. J. Saykally, "Chirped coherent anti-Stokes Raman scattering as a high-spectral and spatial resolution microscopy," Opt. Lett. **32,** 2858 (2007).

[25] R. Glenn, M. Dantus, "Single broadband phase-shaped pulse stimulared Raman spectroscopy for standoff trace explosive detection," J. Phys. Chem. Lett. **7,** 117 (2016).

[26] T. Hellerer, A. M. K. Enejder, A. Zumbusch, "Spectral focusing: High spectral resolution spectroscopy with broad-bandwidth laser pulses," Appl. Phys. Lett. **85,** 25 (2004).

[27] J. X. Cheng, A. Volkmer, X. S. Xie, "Theoretical and experimental characterization of coherent anti-Stokes Raman scattering microscopy," J. Opt. Soc. Am. B **19,** 1363 (2002).

[28] E. S. Manuilovich, V. A. Astapenko, P. A. Golovinskiia, "Propagation of Ultrashort Laser Pulses in Dry and Humid Air", Atmosph. Ocean. Opt., **28,** 209 (2015).

[29] P. Sprangle, J. R. Penano, B. Hafizi, "Propagation of intense short laser pulses in the atmosphere," Phys. Rev. E, **66**, 046418 (2002).

[30] *Analytical Chemistry: An Introduction*, (Saunders Golden Sunburst Series) 7th Ed., by D. A. Skoog, D. M. West, F. J. Holler (1999).

[31] R. Sabatini, M. Richardson, "New techniques for laser beam atmospheric extinction measurements from manned and unmanned aerospace vehicles" Cent. Eur. J. Eng, **3,** 11 (2013).

[32] Y. LeCun, Y. Bengio, G. Hinton, "Deep learning," Nature **521,** 436 (2015).

[33] O. Simeone, " A Brief Introduction to Machine Learning for Engineers," arXiv:1709.02840 [cs.LG] (2018).

[34] D. M. Hawkins, "The Problem of Overfitting" Journal of Chemical Information and Computer Sciences **44 (1)**, 1-12 (2004).

[35] D. Goswami, "Laser Phase Modulation Approaches towards Ensemble Quantum Computing", Phys. Rev. Lett. **88**, 177901 (2002).

[36] G. Liu, S. A. Malinovskaya, "Creation of ultracold molecules within the lifetime scale by direct implementation of an optical frequency comb," J. Mod. Opt., **65**, 1309 (2018).

[37] D. P. Kingma, J. Ba, "Adam: A Method for Stochastic Optimization," arXiv:1412.6980 (2014).

[38] R. Caruana, S. Lawrence, C. L. Giles, "Overfitting in neural nets: Backpropagation, conjugate gradient, and early stopping", In *Advances in Neural Information Processing Systems 13 - Proc. 2000 Conf.* (2001).

[39] V. Nair, G. Hinton, "Rectified Linear Units Improve Restricted Boltzmann Machines," In *Proc. of the 27th Intern. Conf. on Machine Learning,* Haifa, Israel (2010).

[40] K. He, X. Zhang, S. Ren, J. Sun, "Delving Deep into Rectifiers: Surpassing Human-Level Performance on ImageNet Classification," arXiv:1502.01852 (2015).

REPORT DOCUMENTATION PAGE

Form Approved
OMB No. 0704-0188

PLEASE DO NOT RETURN YOUR FORM TO THE ABOVE ORGANIZATION.

1. REPORT DATE *(DD-MM-YYYY)*	2. REPORT TYPE	3. DATES COVERED *(From - To)*
13-06-2023	Final Technical Report	From 03-01-2020-To 02.28.2023

4. TITLE AND SUBTITLE
Quantum-enhanced FAST CARS for remote detection using a multi-static platform

5a. CONTRACT NUMBER

5b. GRANT NUMBER
GRANT12960568

5c. PROGRAM ELEMENT NUMBER

6. AUTHOR(S)
PI: Dr. Svetlana Malinovskaya

5d. PROJECT NUMBER

5e. TASK NUMBER

5f. WORK UNIT NUMBER

7. PERFORMING ORGANIZATION NAME(S) AND ADDRESS(ES)
STEVENS INSTITUTE OF TECHNOLOGY
1 CASTLE POINT ON HUDSON
HOBOKEN NJ 07030-5906
UNITED STATES OF AMERICA

8. PERFORMING ORGANIZATION REPORT NUMBER

9. SPONSORING/MONITORING AGENCY NAME(S) AND ADDRESS(ES)
Office of Naval Research
875 N. Randolph Street, Suite 1425
Arlington, VA 22203-1995

10. SPONSOR/MONITOR'S ACRONYM(S)

11. SPONSOR/MONITOR'S REPORT NUMBER(S)

12. DISTRIBUTION/AVAILABILITY STATEMENT
Public Release

13. SUPPLEMENTARY NOTES

14. ABSTRACT

We propose a new quantum principle based approach for remote detection of hazardous contaminants. It is based on quantum-enabled coherent anti-Stokes Raman scattering (CARS) of laser radiation from the distant molecules in the backward direction. The quantum enhancement is made by implementing quantum control methodology, which maximizes quantum coherence in the target molecules. Coherent signal in the backward direction is sustained by application of phase locked pulse train, which forms an optical frequency comb. The implementation of quantum control methods in combination with optical frequency combs in CARS for remote detection presents a fundamentally new approach within Femtosecond Adaptive Spectroscopic Techniques (FAST CARS). Each pulse in the pulse train is analyzed and controlled using the deep learning algorithm. Deep neural networks are used to analyze the modulation of the phase of the laser fields propagating through the air and aids in making adjustments to the control algorithm for the laser fields. The detection principle relies on the nonlinear optical response of the target molecules, when a blue-shifted with respect to the incident fields radiation is generated coherently in the medium and propagates in a direction defined by the p

15. SUBJECT TERMS

16. SECURITY CLASSIFICATION OF:			17. LIMITATION OF ABSTRACT	18. NUMBER OF PAGES	19a. NAME OF RESPONSIBLE PERSON
a. REPORT	b. ABSTRACT	c. THIS PAGE			19b. TELEPHONE NUMBER *(Include area code)*